Korean J. Chem. Eng., 40(3), 497-503 (2023)
DOI: 10.1007/s11814-022-1227-8

pISSN: 0256-1115
eISSN: 1975-7220

Intertwining porous silicon with conducting polymer for high-efficiency stable Li-ion battery anodes

Jaegeon Ryu*,†, Soojin Park, Dongki Hong***, and Sunghee Shin*****

*Department of Chemical and Biomolecular Engineering, Sogang University, Seoul 04107, Korea
**Department of Chemistry, Division of Advanced Materials Science,
Pohang University of Science and Technology (POSTECH), Pohang 37673, Korea
***Department of Energy Engineering, School of Energy and Chemical Engineering,
Ulsan National Institute of Science and Technology (UNIST), Ulsan 44919, Korea
(*Received 9 June 2022 • Revised 7 July 2022 • Accepted 10 July 2022*)

Abstract−Porous silicon anodes have been extensively investigated for the high-performance lithium-ion battery, owing to their high capacity and structural robustness as dominantly incorporated with conductive carbon sheath. However, the typical high-temperature annealing process for carbon coating induces the collapse of pre-engineered pores and limits the full utilization of porous structures. In this work, porous silicon flake intertwined with doped polyaniline was prepared via redox-transmetalation reaction followed by a wet coating process of conducting polymer. The proposed method eliminates the risk of pore collapse and utilizes the conductive network without compromising the porous structure. As a result, the prepared composite consisting of porous silicon flake and doped polyaniline shows an extended battery cycle life, reduced electrode swelling, and increased efficiency.

Keywords: Porous Silicon, Conducting Polymers, Doping, Anodes, Lithium-ion Batteries

INTRODUCTION

The imperative to boost the energy density of lithium-ion batteries (LIBs) has been hindered by the limited materials library to replace the commercialized intercalation anodes and cathodes [1]. Particularly, lithium storage in the stacking structure of graphene, i.e., graphite, ensures the structural stability of the host while suffering from sluggish site-specific diffusion of Li-ion toward the graphite anode and low utilization of honey comb carbon sites (C_6Li≈ 370 mAh/g) [2]. Apart from the intercalation-type redox reaction, alloying-type group IV elements, as represented by silicon (Si), hold great potential due to their high theoretical capacity (>3,000 mAh/g) and earth abundance [3]. However, extensive lithiation (lithium intake) of Si anodes causes more than 300% of volume expansion followed by crack formation on the surface. Consequently, the interface structure of the Si anode is vulnerable to fracture and loses the ionic pathway, and more severe electrical isolation of active materials takes place [4].

Reducing the feature size of Si anode, so-called nanostructuring, has led to groundbreaking findings in that there is a critical size (less than 150 nm) for the non-fracture behavior of Si anode during electrochemical cycling [5], thus extending the battery cycle life. Despite costly production methods for the nanostructured materials, the structural design at the nanoscale, such as nanosheets, nanowires, and nanotubes, has been extensively studied and demonstrated as one of the most feasible solutions [6-15]. In addition, introducing a porosity to the Si anodes provides sufficient room for inward breathing and significantly lowers the risk of fracture as validated by theoretical and experimental observations [12,16-18]. Sustainable (hierarchical) porosity throughout the electrochemical cycles serves as Li-ion diffusion channels as enhancing the rate performance of batteries. Thus, nanostructured Si anodes incorporated with a reasonable level of porosity are highly desirable for the development of high-energy-density LIBs [19].

Structural control of Si-based anodes has still been plagued by the low electrical conductivity of semiconducting Si, which inevitably calls for compositing with conductive carbon sheath in primary or secondary processing [4,20-23]. Layering the conductive carbons onto the diverse Si anodes not only provides an electronic conduction pathway, but also passivates the reactive surface toward the liquid electrolyte, thereby improving the interface stability of Si anodes. Thus, the supportive carbon layers buffer the huge stress of Si anodes during the lithium intake and extraction process and promote the formation of a stable solid-electrolyte-interphase (SEI) layer. Passivation of Si anodes with uniform carbon layers typically follows high-temperature annealing (>700 °C) of gaseous precursors which generated either graphitic or non-graphitic carbons [10,24-26]. Unfortunately, the pre-engineered pores and nanostructures collapse during the high-temperature treatment, which indicates that the conductive sheath needs to be fully impregnated with a minimized (or no) thermal effect on the structure [27]. Instead, conducting polymers can lower the thermal stress onto the Si materials while maintaining the electrical conductivity of the electrode in the form of either binder, electrolytes, or protective layers [28-31].

Herein, we report the preparation of doped polyaniline coated porous silicon flake anode (pSi-dPAni) for the LIB anode via redox-

†To whom correspondence should be addressed.
E-mail: jryu@sogang.ac.kr
Copyright by The Korean Institute of Chemical Engineers.

transmetalation reaction followed by solution coating of conducting polymer without any critical thermal stress onto the pre-engineered Si structures. This strategy is fully coupling the nanostructured porous Si anode with conductive sheath/buffer to improve the electrode integrity, cycle life, rate performance and, most importantly, Coulombic efficiency of batteries.

EXPERIMENTAL

1. Preparation of pSi

The pSi was prepared following the procedure reported in our previous work [32]. Typically, clay mineral (talc, SAMCHUN) and magnesium powder (size of less than 10 μm) were uniformly mixed using ethanol as a solvent. Then, the dried mixture was placed inside a tube furnace filled with Ar gas and heated to 650 °C for 3 hours. After natural cooling, the as-reduced products were rinsed with deionized (DI) water and 1.0 M HCl solution to obtain the pSi samples.

2. Preparation of pSi-dPAni

To prepare the pSi-dPAni, 1 g of pSi was first dispersed in 50 mL of ethanol using a tip sonicator at least for 10 mins. Afterward, the predetermined amounts of aniline precursor (0.1 mL, ≥99.5%, Sigma-Aldrich) were added to the dispersion followed by an additional 10-min-sonication. Finally, ammonium sulfate (0.3 g) and 1.0 M HCl aqueous solution (20 mL) were slowly added to the mixture and vigorously stirred for 5 hours to ensure the complete polymerization onto the pSi. The polyaniline-coated pSi samples were collected by vacuum filtration with excessive DI water/ethanol washing (pSi-PAni). To de-dope the pSi-PAni, it was first dispersed in ethanol and then 1.0 M sodium hydroxide aqueous solution was added to the dispersion. The obtained de-doped sample using vacuum filtration was again dispersed in ethanol and 1.0 M camphorsulfonic acid (CSA, 20 mL, 98%, Sigma-Aldrich)) was added to introduce the SO_3^- doping into the de-doped sample (pSi-dPAni).

3. Materials Characterization

Microstructural analysis of the samples was confirmed by scanning electron microscopy (SEM, JSM-700F Prime, JEOL) equipped with energy-dispersive spectroscopy (EDS) and high-resolution scanning-transmission electron microscopy (HR-STEM, 2100F with Cs corrected STE, JEM-2100F, JEOL). Thermogravimetric analysis (Q500, TA) and elemental analysis (Truspec Micro, Leco) were employed to calculate the elemental composition of the samples. The surface functionality and functional groups of polymers were characterized by using Fourier-transform infrared (FT-IR, 670, Varian). The pore structure of the samples was characterized using surface area and pore size analyzer (BELSORP-mini II, BEL Japan, Inc.).

4. Electrochemical Characterization

The pSi and pSi-dPAni samples electrode consist of active powders, poly(acrylic acid)/sodium carboxymethyl cellulose (PAA/CMC 1/1 w/w) binder, and Super-P as a conducting agent with a weight ratio of 80 : 10 : 10. The mixed aqueous slurry was cast on Cu current collector, dried at 150 °C for 2 hours under vacuum, and used as working electrodes with Li foil as the counter/reference electrode and Celgard 2400 membrane as the separator. The graphite blending electrode was prepared to achieve 750 mAh/g of a reversible specific capacity at the initial cycle. The loading level of electrodes was maintained at 0.5-1.0 mg cm^{-2} and 2.0-2.5 mg cm^{-2} for pSi-dPAni and graphite blending electrodes, respectively. The pSi-dPAni/Graphite electrode was calendared at an electrode density of 1.0-1.2 g/cc. Electrochemical test was evaluated by using a 2032 coin-type cell fabricated inside an argon-filled glove box. The electrolyte was 1.3 M lithium hexafluorophosphate ($LiPF_6$) in 3/7 (w/w) ethylene carbonate (EC)/diethylene carbonate (DEC) containing 10 wt% fluoroethylene carbonate (FEC). Galvanostatic charge/discharge tests were carried out with WBCS 3000 (WonAtech) testing instrument in a voltage range from 0.005 to 1.5 V (formation cycle at 0.05 C) and from 0.01 to 1.0 V (subsequent cycles starting at 0.1 C). The cycle retention and rate capability for the pSi-dPAni electrodes were tested at 0.33 C and 0.1-5.0 C, respectively. The cycle retention for the pSi-dPAni/Graphite electrode was tested at 0.5 C. For post-mortem analysis, the cycled cells were disassembled inside an argon-filled glove box and then washed with dimethyl carbonate (DMC) to remove residual electrolytes.

RESULTS AND DISCUSSION

The preparation of porous Si flake (pSi) follows a well-designed redox-transmetalation reaction as reported previously [32]. At well above the melting point (650 °C) of the reducing agent, melted or vaporized Mg metals attack the surface oxygen sites of clay minerals. During successive reduction processes, interior magnesium oxide layers sandwiched by two adjacent silicate layers scavenge substantial exothermic heat as a negative catalyst to retain the original flake structure without the use of typical metal salts [33]. Afterward, a large portion of magnesium oxide is etched out from the initial clay flakes, thus leaving large void spaces and multiscale pores. Among various types of porous Si materials, this porous Si flake has been selected as a model system to introduce the conducting polymer layers, since this hyperporous structure enables the full coverage of the surface as well as the intertwining of polymeric materials.

Prior to coating the conducting polymers, the surface of pSi

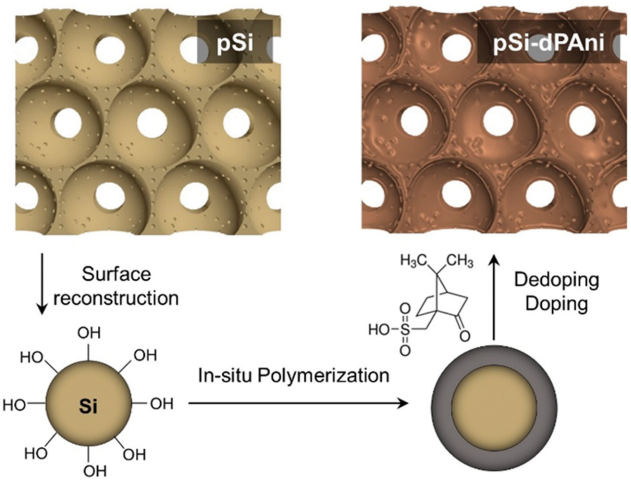


Fig. 1. Schematic of preparation for doped polyaniline-intertwined porous Si flake (pSi-dPAni).

needs to be polished by treating it with hydrofluoric acid to eliminate the excessive oxide layers (Fig. 1). The naturally formed passivation layer with surficial hydroxyl groups is desirable for further functionalization [34]. On the active surface of pSi, the monomers (i.e., aniline) are oxidatively in-situ polymerized in the presence of a strong acid and initiated by an oxidant [35,36]. The coating amounts can be readily tunable by the relative weight fraction of pSi to aniline. However, the control of such coating thickness is out of discussion in this study, and instead, the doping effect of polyaniline (PAni) on the battery performance of Si anodes is the most important concern. The polyaniline-coated pSi samples are de-doped by sodium hydroxide treatment and finally, the sulfonic acid group (SO_3^-) from the camphorsulfonic acid (CSA) is doped into the polyaniline (pSi-dPAni). It is noted that doping the PAni with nucleophiles increased the electrical conductivity of the polymer and such groups improved the adhesion property with polymeric binders in the composite electrode [37].

The initial non-porous and highly-stacked flake structure of clay minerals was transformed into the highly porous Si flake, which is either single-layer or multi-stacked via redox-transmetalation reaction (Fig. 2(a), (b)). The pore diameters range from 100 nm to 200 nm and the width of the flake is approximately 2-4 μm. The introduction of doped polyaniline leads to partially agglomerated pSi structures and the macropores of the flake partly diminish, which indicates the fine control of surface coating layers (Fig. 2(c)). The thickness of both pSi and pSi-dPAni samples can be estimated as 150 nm in average (inset of Fig. 2(b), (c)). In addition, energy-dispersive X-ray spectroscopy (EDS) results reveal that outer surface layers consist of mainly carbon, oxygen, and nitrogen, which is consistent with the presence of polyaniline and sulfonic acid groups, respectively (Fig. 2(d), (e)). It is less likely that the dense oxygen map of pSi-dPAni samples originates from the passivation layer due to the pretreatment of pSi with hydrofluoric acid. Note that negligible amounts of sulfur atoms in doping agents are hardly detected from the EDS analysis. Further, the thermogravimetric analysis shows that the composite structure includes approximately 8.0 wt% of the doped polyaniline (Fig. 2(f)). The rapid ramping of temperature under the airflow causes a slight shift of the onset temperature of PAni decomposition, while a rise after the drastic weight loss indicates the complete thermal decomposition of PAni followed by oxidation of pSi.

As etching out the reduction byproducts, transmission electron microscopy (TEM) analysis reveals that the pSi flakes feature regular macropores and minor meso-/micropores on the framework as reported previously as shown in Fig. 3(a) [32]. In addition, a high-resolution TEM image shows a clear edge of macropores and a well-defined crystalline structure of Si (inset of Fig. 3(a)). After coating with dPAni, the size of initial macropores in pSi flakes is greatly reduced but not fully collapsed. Importantly, the surface of the pSi flake is uniformly coated (average thickness of coating layer: 7-8 nm) with a dPAni layer without severe agglomeration of polymers, thus rendering the surface of Si amorphous (Fig. 3(b)). In addition, nitrogen adsorption results show that substantial amounts of pores are collapsed after the dPAni coating as featuring the Brauner-Emmet-Teller (BET) surface area of 188 m^3/g and 42.8 m^3/g for pSi and pSi-dPAni samples, respectively (Fig. 3(c)). Multiscale pores, which range from 1-150 nm in the pSi sample, are fully covered with dPAni layer to exhibit the disappearance of the majority of pores in the pore size distribution curves (Fig. 3(d)). Despite the decreased apparent porosity in the measurement, the multiscale porous structure of Si was retained underneath the dPAni layer, which is consistent with TEM results above.

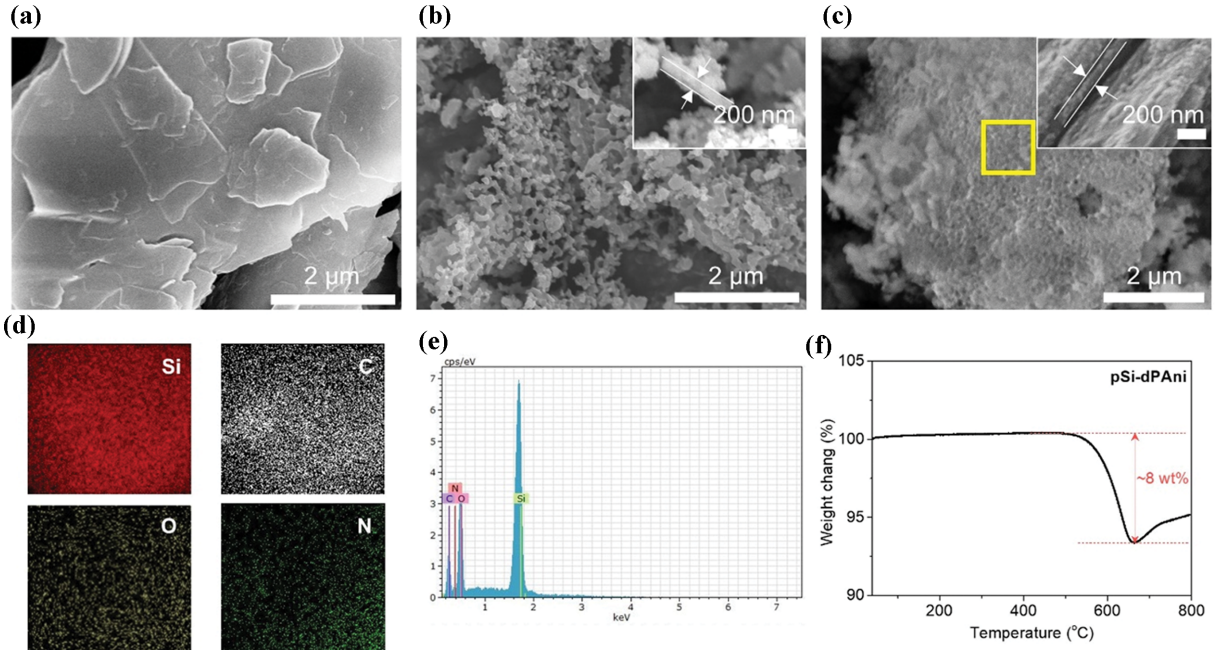


Fig. 2. SEM images of (a) bare clay minerals, (b) porous silicon flake (pSi) and (c) pSi-dPAni (inset: high-magnification SEM images to show the thickness of the samples). (d) EDS elemental maps, and (e) the corresponding EDS spectrum for the selected area in (c). (f) TGA result of pSi-dPAni.

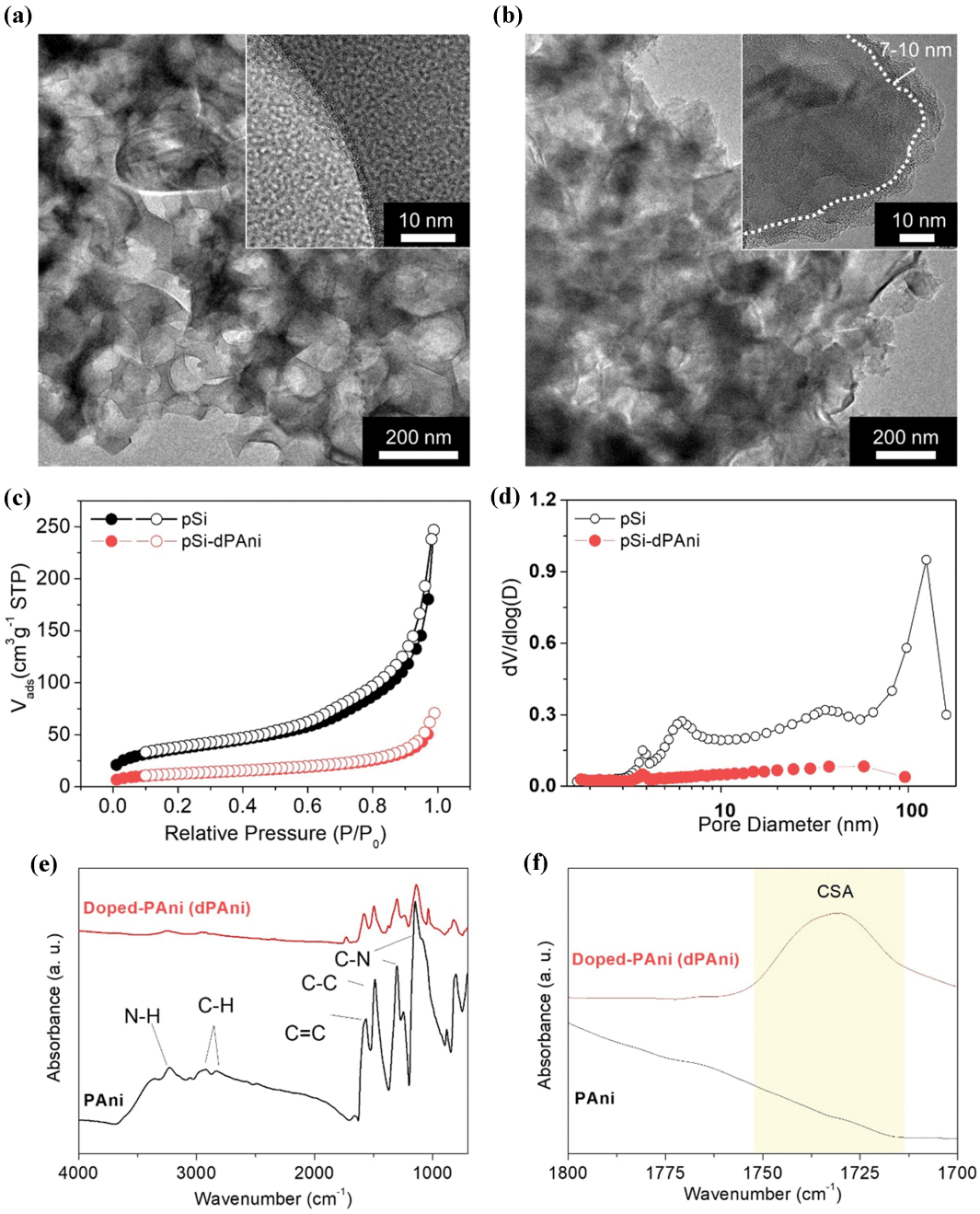


Fig. 3. TEM images of (a) pSi and (b) pSi-dPAni (inset: high-magnification TEM images). (c) Nitrogen adsorption-desorption isotherm curves and (d) Pore size distribution curves for pSi and pSi-dPAni. (e), (f) FT-IR spectra of bare PAni and doped PAni (dPAni) (Note: CSA-camphorsulfonic acid). Nitrogen sorption results for pSi have been reproduced with permission [32].

To confirm the surface functionality and presence of dopants, the PAni samples were separately prepared (Fig. 3(e), (f)). The FT-IR spectra of PAni before and after doping both show characteristic peaks for PAni, which can be assigned to the secondary amine (R-NH-R) and benzene ring. However, doping with camphorsulfonic acid induced the distinctive evolution of new peaks at 1,710-1,750 cm^{-1}, which strongly implies the presence of sulfonic acid groups and different carbonyl moieties [38]. Thus, the dopants are strongly coordinated to the conjugated structure of PAni, and this complex structure of polymer seamlessly envelops the multiscale porous Si flakes.

The electrochemical evaluation of the pSi-dPAni and pSi samples was performed by assembling the CR2032 coin cells using Li metal as a counter/reference electrode and a typical carbonate electrolyte (see details in the experimental section). Galvanostatic discharge (lithiation)-charge (delithiation) curves at the first cycle show that both pSi and pSi-dPAni electrodes deliver a reversible capacity as high as 2,720 and 3,020 mAh/g along with initial Coulombic efficiency (ICE) of 92.2% and 93.1%, respectively, which are both record-breaking values among various Si designs (Fig. 4(a))

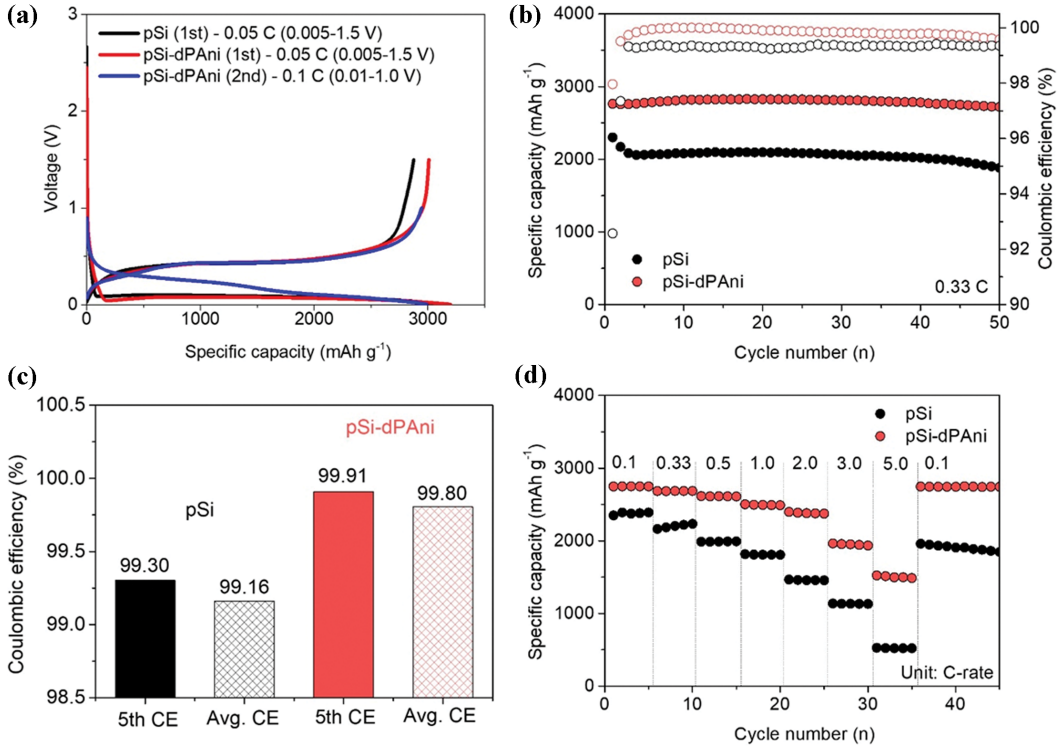


Fig. 4. Battery performance of pSi and pSi-dPAni electrodes. (a) Galvanostatic discharge-charge curves, (b) capacity retention and corresponding Coulombic efficiency at 0.33 C, (c) charted Coulombic efficiency at the 5th cycle and for 50 cycles, and (d) rate capability results of pSi and pSi-dPAni electrodes.

[39]. The enhancement of charge capacity and ICE is contributed to the reduced porosity (surface area) and the increased conductivity throughout the flake framework [40]. The physical barrier consisting of ion-conductive PAni structure serves as a kind of artificial SEI, while the low-temperature coating of conductive materials onto the Si retains the pre-engineered structural effects from pSi. In our previous study, pSi with an amorphous carbon layer prepared via the chemical vapor deposition (CVD) method showed a similar improvement, but their ICE was slightly lower than that of the pSi-dPAni sample [32]. It is assumed that the conductive network derived from the dPAni constructs a more sustainable structure after the electrode fabrication due to the densely packed conductive materials into the pores and the interaction of coating layers with polymeric binders.

The conductive buffer (i.e., dPAni) not only improves the structural stability of the pSi sample but also shows an outstanding rate capability (Fig. 4(b), (d)). Despite the relatively insufficient mechanical strength of PAni compared to other polymeric materials or even CVD-grown amorphous carbon, the dopants in the PAni facilitate the formation of a sustainable electrode network to extend the battery cycle life (capacity retention of 99% vs. 89% after 50 cycles at 0.33 C) [41]. Synergistic coupling of multiscale porous Si flakes and dPAni significantly increases the Coulombic efficiency (CE) during the subsequent cycles. The CE per cycle is the most crucial barometer to determine the cycle life of traditional and next-generation batteries [42]. Ideally, quick saturation of CE over 99.9% is highly desired, but even 99.9% of average CE during the cycles could retain only 80% of initial capacity after 200 cycles. In this respect, the measurement of CE per cycle must take precedence for developing the practical anodes. When introducing dPAni into the pSi samples, the CE reaches 99.91% just after five discharge-charge cycles, while the native pSi electrode shows 99.30% and the average CE for 50 cycles is much lower than 99.5% (Fig. 4(c)). This result indicates that the prepared pSi-dPAni is a promising candidate for further evaluation in the graphite-blending cells, which are typical procedures for fabricating the commercial electrodes [43].

The improved battery performance is consistent with the post-mortem analysis of electrodes. For the pSi, the electrode was significantly swollen out (~191%) after 100 cycles, while the pSi-dPAni showed a limited swelling of 85% at a capacity loading of >2.0 mAh cm^{-2} (Fig. 5(a)-(d)). The porosity of the pSi electrode completely diminished, although there was plenty of material-level porosity before cycles. Thus, even elaborately controlled Si materials might suffer from a structural collapse in an early stage of cycling. To validate the practical feasibility of the pSi-dPAni sample, the graphite-blending electrode (pSi-dPAni/Graphite) was formulated at a target charge capacity of 750 mAh/g. Impressively, the pSi-dPAni/Graphite electrode shows an ICE of 93.0%, which is comparable to conventional pure graphite electrode (89-94%) as shown in Fig. 5(e) [44]. In subsequent cycles, the CEs were quickly saturated to 99.9% after three discharge-charge cycles. Moreover, the blending electrode shows a negligible polarization upon the increased current density and retains more than 90% of the initial capacity after 300 cycles along with zero swelling after cycles (Fig. 5(f)-(h)), thus demonstrating superior feasibility of the pSi-dPAni sample toward the development of practical anodes.

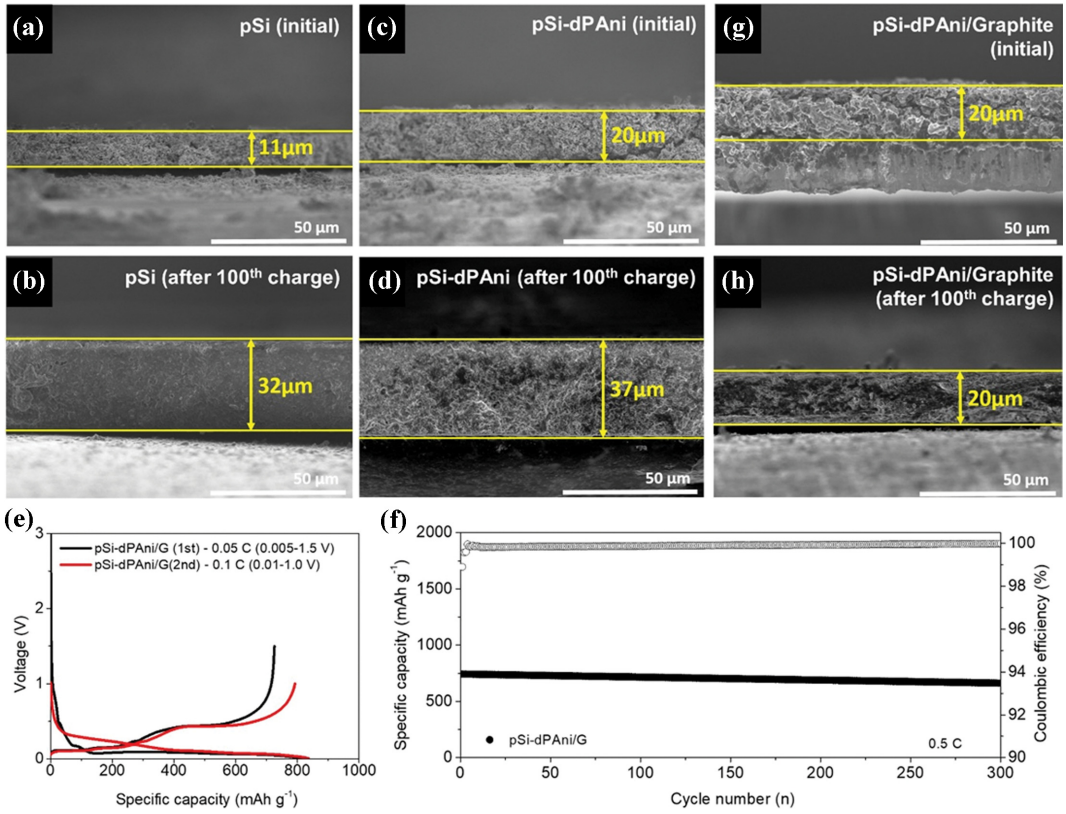


Fig. 5. SEM images of pSi (a), (b), pSi-dPAni (c), (d), and pSi-dPAni/Graphite (g), (h) electrodes before cycle and after 100th charge, respectively. (e) Galvanostatic discharge-charge curves and (f) capacity retention and corresponding Coulombic efficiency at 0.5 C for pSi-dPAni/Graphite electrode.

CONCLUSIONS

A composite anode comprising porous Si flake and doped polyaniline was prepared by scalable redox-transmetalation reaction and solution coating process and evaluated as the anode for LIB. The resulting pSi-dPAni showed promising electrochemical performance by combining the effects of porous structure and conductive buffers. Compared to the conventional method of introducing conductive carbon layers onto Si via thermal annealing, the proposed here eliminates the thermal stress effect on the porous structure and fully retains the initial nanostructures, thus improving the battery cycle life, rate capability, and (initial) Coulombic efficiency. This work sheds light on the development of Si-polymer composite anode for practical applications.

ACKNOWLEDGEMENTS

This work was supported by the Sogang University Research Grant of 202210028.01.

REFERENCES

1. R. Schmuch, R. Wagner, G. Hörpel, T. Placke and M. Winter, *Nat. Energy*, **3**, 267 (2018).
2. L. Zhao, B. Ding, X.-Y. Qin, Z. Wang, W. Lv, Y.-B. He, Q.-H. Yang and F. Kang, *Adv. Mater.*, **34**, 2106704 (2022).
3. H. Wu and Y. Cui, *Nano Today*, **7**, 414 (2012).
4. J. Ryu, D. Hong, H.-W. Lee and S. Park, *Nano Res.*, **10**, 3970 (2017).
5. X. H. Liu, L. Zhong, S. Huang, S. X. Mao, T. Zhu and J. Y. Huang, *ACS Nano*, **6**, 1522 (2012).
6. C. K. Chan, H. Peng, G. Liu, K. McIlwrath, X. F. Zhang and R. A. Huggins and Y. Cui, *Nat. Nanotechnol.*, **3**, 31 (2008).
7. H. Wu, G. Chan, J. W. Choi, I. Ryu, Y. Yao, M. T. McDowell, S. W. Lee, A. Jackson, Y. Yang, L. Hu and Y. Cui, *Nat. Nanotechnol.*, **7**, 310 (2012).
8. J. Ryu, D. Hong, S. Choi and S. Park, *ACS Nano*, **10**, 2843 (2016).
9. Y. Yao, M. T. McDowell, I. Ryu, H. Wu, N. Liu, L. Hu, W. D. Nix and Y. Cui, *Nano. Lett.*, **11**, 2949 (2011).
10. J. Ryu, T. Chen, T. Bok, G. Song, J. Ma, C. Hwang, L. Luo, H.-K. Song, J. Cho, C. Wang, S. Zhang and S. Park, *Nat. Commun.*, **9**, 2924 (2018).
11. B. Chen, L. Chen, L. Zu, Y. Feng, Q. Su, C. Zhang and J. Yang, *Adv. Mater.*, **34**, 2200894 (2022).
12. J. Ryu, J. H. Seo, G. Song, K. Choi, D. Hong, C. Wang, H. Lee, J. H. Lee and S. Park, *Nat. Commun.*, **10**, 2351 (2019).
13. U. Kasavajjula, C. Wang and A. J. Appleby, *J. Power Sources*, **163**, 1003 (2007).
14. M. Ko, S. Chae, J. Ma, N. Kim, H.-W. Lee, Y. Cui and J. Cho, *Nat. Energy*, **1**, 16113 (2016).
15. J. Ryu, M. Je, W. Choi and S. Park, *Mater. Adv.*, **1**, 2797 (2020).
16. Q. Xiao, M. Gu, H. Yang, B. Li, C. Zhang, Y. Liu, F. Liu, F. Dai, L. Yang, Z. Liu, X. Xiao, G. Liu, P. Zhao, S. Zhang, C. Wang, Y. Lu and

M. Cai, *Nat. Commun.*, **6**, 8844 (2015).
17. H. Kim, B. Han, J. Choo and J. Cho, *Angew. Chem. Int. Ed.*, **47**, 10151 (2008).
18. D. Hong, J. Ryu, S. Shin and S. Park, *J. Mater. Chem. A*, **5**, 2095 (2017).
19. H. Jia, X. Li, J. Song, X. Zhang, L. Luo, Y. He, B. Li, Y. Cai, S. Hu, X. Xiao, C. Wang, K. M. Rosso, R. Yi, R. Patel and J.-G. Zhang, *Nat. Commun.*, **11**, 1474 (2020).
20. W. Wang and P. N. Kumta, *ACS Nano*, **4**, 2233 (2010).
21. Z. Lu, N. Liu, H.-W. Lee, J. Zhao, W. Li, Y. Li and Y. Cui, *ACS Nano*, **9**, 2540 (2015).
22. R. Yi, F. Dai, M. L. Gordin, S. Chen and D. Wang, *Adv. Energy Mater.*, **3**, 295 (2013).
23. J. Ryu, T. Bok, S. H. Joo, S. Yoo, G. Song, S. H. Kim, S. Choi, H. Y. Jeong, M. G. Kim, S. J. Kang, C. Wang, S. K. Kwak and S. Park, *Energy Storage Mater.*, **36**, 139 (2021).
24. I. H. Son, J. H. Park, S. Kwon, S. Park, M. H. Rümmeli, A. Bachmatiuk, H. J. Song, J. Ku, J. W. Choi, J.-m. Choi, S.-G. Doo and H. Chang, *Nat. Commun.*, **6**, 7393 (2015).
25. Y.-C. Zhang, Y. You, S. Xin, Y.-X. Yin, J. Zhang, P. Wang, X.-s. Zheng, F.-F. Cao and Y.-G. Guo, *Nano Energy*, **25**, 120 (2016).
26. W. An, B. Gao, S. Mei, B. Xiang, J. Fu, L. Wang, Q. Zhang, P. K. Chu and K. Huo, *Nat. Commun.*, **10**, 1447 (2019).
27. S. Chae, Y. Xu, R. Yi, H.-S. Lim, D. Velickovic, X. Li, Q. Li, C. Wang and J.-G. Zhang, *Adv. Mater.*, **33**, 2103095 (2021).
28. T. M. Higgins, S.-H. Park, P. J. King, C. Zhang, N. McEvoy, N. C. Berner, D. Daly, A. Shmeliov, U. Khan, G. Duesberg, V. Nicolosi and J. N. Coleman, *ACS Nano*, **10**, 3702 (2016).
29. H. Wu, G. Yu, L. Pan, N. Liu, M. T. McDowell, Z. Bao and Y. Cui, *Nat. Commun.*, **4**, 1943 (2013).
30. Y. Yao, N. Liu, M. T. McDowell, M. Pasta and Y. Cui, *Energy Environ. Sci.*, **5**, 7927 (2012).
31. H.-Y. Lin, C.-H. Li, D.-Y. Wang and C.-C. Chen, *Nanoscale*, **8**, 1280 (2016).
32. J. Ryu, D. Hong, M. Shin and S. Park, *ACS Nano*, **10**, 10589 (2016).
33. K. Nishiyama, T. Ono, A. Nakayama, H. Sakai, M. Koishi and M. Abe, *Surf. Coat. Int. B: Coat. Trans.*, **86**, 169 (2003).
34. J. M. Kim, S. M. Chang, S. M. Kong, K.-S. Kim, J. Kim and W.-S. Kim, *Ceram. Int.*, **35**, 1015 (2009).
35. S.-J. Tang, A.-T. Wang, S.-Y. Lin, K.-Y. Huang, C.-C. Yang, J.-M. Yeh and K.-C. Chiu, *Polym. J.*, **43**, 667 (2011).
36. M. Kummer, J. P. Badillo, A. Schmitz, H. G. Bremes, M. Winter, C. Schulz and H. Wiggers, *J. Electrochem. Soc.*, **161**, A40 (2013).
37. K. Bednarczyk, W. Matysiak, T. Tański, H. Janeczek, E. Schab-Balcerzak and M. Libera, *Sci. Rep.*, **11**, 7487 (2021).
38. P. Sangeetha, S. Mullainathan, S. Muthu, B. R. Rajaraman, A. Saral and S. Selvakumari, *Mater. Today: Proc.*, **50**, 2768 (2022).
39. B. Zhu, G. Liu, G. Lv, Y. Mu, Y. Zhao, Y. Wang, X. Li, P. Yao, Y. Deng, Y. Cui and J. Zhu, *Sci. Adv.*, **5**, eaax0651 (2019).
40. J. B. Cook, H.-S. Kim, T. C. Lin, S. Robbennolt, E. Detsi, B. S. Dunn and S. H. Tolbert, *ACS Appl. Mater. Interfaces*, **9**, 19063 (2017).
41. H. Valentová and J. Stejskal, *Synth. Met.*, **160**, 832 (2010).
42. J. Xiao, Q. Li, Y. Bi, M. Cai, B. Dunn, T. Glossmann, J. Liu, T. Osaka, R. Sugiura, B. Wu, J. Yang, J.-G. Zhang and M. S. Whittingham, *Nat. Energy*, **5**, 561 (2020).
43. S. Chae, N. Kim, J. Ma, J. Cho and M. Ko, *Adv. Energy Mater.*, **7**, 1700071 (2017).
44. G. Song, J. Ryu, S. Ko, B. M. Bang, S. Choi, M. Shin, S.-Y. Lee and S. Park, *Chem. Asian J.*, **11**, 1711 (2016).